(2)

NAVAL POSTGRADUATE SCHOOL
Monterey, California

THESIS

MAGNETIC FIELD MEASUREMENTS OF THE CEBAF (NIST) WIGGLER USING THE PULSED WIRE METHOD

by

Stephen M. Wallace

September, 1992

Thesis Advisor: William B. Colson
Thesis Co-Advisor: George R. Neil

UNCLASSIFIED
SECURITY CLASSIFICATION OF THIS PAGE

REPORT DOCUMENTATION PAGE

Form Approved
OMB No 0704-0188

1a REPORT SECURITY CLASSIFICATION UNCLASSIFIED	1b RESTRICTIVE MARKINGS NONE
2a SECURITY CLASSIFICATION AUTHORITY N/A	3 DISTRIBUTION/AVAILABILITY OF REPORT APPROVED FOR PUBLIC RELEASE; DISTRIBUTION IS UNLIMITED
2b DECLASSIFICATION/DOWNGRADING SCHEDULE N/A	
4 PERFORMING ORGANIZATION REPORT NUMBER(S) N/A	5 MONITORING ORGANIZATION REPORT NUMBER(S) N/A
6a NAME OF PERFORMING ORGANIZATION NAVAL POSTGRADUATE SCHOOL 6b OFFICE SYMBOL (If applicable) 33	7a NAME OF MONITORING ORGANIZATION NAVAL POSTGRADUATE SCHOOL
6c. ADDRESS (City, State, and ZIP Code) MONTEREY, CA 93943-5000	7b ADDRESS (City, State, and ZIP Code) MONTEREY, CA 93943-5000
8a NAME OF FUNDING/SPONSORING ORGANIZATION N/A 8b. OFFICE SYMBOL (If applicable) N/A	9 PROCUREMENT INSTRUMENT IDENTIFICATION NUMBER N/A
8c. ADDRESS (City, State, and ZIP Code) N/A	10 SOURCE OF FUNDING NUMBERS PROGRAM ELEMENT NO: N/A; PROJECT NO: N/A; TASK NO: N/A; WORK UNIT ACCESSION NO: N/A
11 TITLE (Include Security Classification) MAGNETIC ERROR MEASUREMENT OF THE CEBAF (NIST) WIGGLER USING THE PULSED WIRE METHOD (UNCLAS)	
12. PERSONAL AUTHOR(S) WALLACE, STEPHEN M.	
13a TYPE OF REPORT MASTER'S THESIS 13b TIME COVERED FROM _____ TO _____	14 DATE OF REPORT (Year, Month, Day) SEP 92 15 PAGE COUNT 51
16 SUPPLEMENTARY NOTATION THE VIEWS EXPRESSED IN THIS THESIS ARE THOSE OF THE AUTHOR AND DO NOT REFLECT THE OFFICAL POLICY OR POSITION OF THE DEPARTMENT OF DEFENSE OR THE U.S. GOVERNMENT	
17 COSATI CODES FIELD / GROUP / SUB-GROUP	18 SUBJECT TERMS (Continue on reverse if necessary and identify by block number) FREE ELECTRON LASER (FEL);PULSED WIRE METHOD; HIGH ENERGY LASER (HEL);SHIPBOARD HIGH ENERGY LASER; THEATER BALLISTIC MISSILE DEFENSE (TBMD)

19 ABSTRACT (Continue on reverse if necessary and identify by block number)

The Free Electron Laser (FEL) has proven to be a versatile photon source for many applications in science, industry and defense. It is capable of providing wide tunability and high efficiency, but has yet to yield high average power required as a weapon system. The proposed infrared and ultraviolet FELs at the Continuous Electron Beam Accelerator Facility (CEBAF) have been projected to provide high average power.

The first section of this thesis will study the necessity of a FEL for shipboard defense, and state the advantages over other defense systems. The remainder will focus on use of the pulsed wire method for measuring the magnetic field errors of the CEBAF/National Institute of Science and Technology (NIST) wiggler. Data analysis indicates the wiggler will have a net electron beam deflection of x=5.2mm, which is much greater than the electron beam radius of r_e=0.4mm and the optical mode waist of w_0=1mm.

20 DISTRIBUTION/AVAILABILITY OF ABSTRACT ☒ UNCLASSIFIED/UNLIMITED ☐ SAME AS RPT ☐ DTIC USERS	21 ABSTRACT SECURITY CLASSIFICATION UNCLASSIFIED
22a NAME OF RESPONSIBLE INDIVIDUAL W. B. Colson	22b TELEPHONE (Include Area Code) (408)646-2765 22c OFFICE SYMBOL PH/Cw

DD Form 1473, JUN 86 *Previous editions are obsolete*

S/N 0102-LF-014-6603

SECURITY CLASSIFICATION OF THIS PAGE
UNCLASSIFIED

Approved for public release; distribution is unlimited

MAGNETIC FIELD MEASUREMENTS OF THE CEBAF (NIST) WIGGLER USING THE PULSED WIRE METHOD

by

Stephen M. Wallace

Lieutenant, United States Navy
B.S., San Jose State University, 1986

Submitted in partial fulfillment of the
requirements for the degree of

MASTER OF SCIENCE IN PHYSICS

from the

NAVAL POSTGRADUATE SCHOOL

September, 1992

Author: _____
Stephen M. Wallace

Approved by: _____
William B. Colson, Thesis Co-Advisor

_____
George R. Neil, Thesis Co-Advisor

_____
Karlheinz E. Woehler, Chairman,
Department of Physics

ABSTRACT

The Free Electron Laser (FEL) has proven to be a versatile photon source for many applications in science, industry and defense. It is capable of providing wide tunability and high efficiency, but has yet to yield the high average power required as a weapon system. The proposed infrared and ultraviolet FELs at the Continuous Electron Beam Accelerator Facility (CEBAF) have been projected to provide high average power.

The first section of this thesis will study the necessity of a FEL for shipboard defense, and state the advantages over other defense systems. The remainder will focus on use of the pulsed wire method for measuring the magnetic field errors of the CEBAF/National Institute of Science and Technology (NIST) wiggler. Data analysis indicates the wiggler will have a net electron beam deflection of $\Delta x \approx 5.2$ mm, which is much greater than the electron beam radius of $r_e \approx 0.4$ mm and the optical mode waist of $w_o \sim 1$ mm.

TABLE OF CONTENTS

I. INTRODUCTION

Free Electron Lasers (FELs) were introduced conceptually in 1971 [1], with successful experiments of the FEL amplifier in 1976 [2] and the FEL oscillator in 1977 [3]. An FEL is unique among lasers since its wavelength is tunable over an order of magnitude — a range much broader than traditional dye or gas lasers. In fact, the FEL lasing wavelengths are limited primarily by the resonator optics, which normally have narrow bandwidths. The FEL also shows promise for high average power and efficiency, with output in the megawatt range and high wallplug efficiencies. Because of these properties, FELs have been proposed for many scientific, industrial and military applications.

Computer manufacturers, for example, are interested in the FEL for lithographic manufacturing of computer memory chips [4]. Currently, 16-Megabit (MB) chips with a 0.5 μm component spacing have been manufactured using optical lithography techniques. Since the projection resolution increases with decreasing wavelength, a short wavelength light source will allow component spacing to be further reduced, and possibly lead to a 1-GB chip with a linespacing of less than 0.1 μm [4]. Research is being conducted to develop photoresists and photomasks with absorption ranges matching currently available lasers. The FEL would greatly simplify this research since the FEL output wavelength is tunable, so the FEL would be constructed to take advantage of common photoresists. Large volume computer chip manufacturing would make the high initial capital investment for a FEL feasible.

The FEL is also a candidate for other uses, such as nuclear fusion [5], reprocessing of spent nuclear fuel [4], medical applications [4], and ballistic missile defense [6, 7, 8].

Chapter II discusses the use of the FEL for ballistic missile defense onboard Navy ships in light of the current proliferation of modern cruise and ballistic missiles to the third-world. The Mid Infrared Advanced Chemical Laser (MIRACL) laser, and the High Energy Laser Weapons System (HELWEPS), a MIRACL-based weapon system for shipboard use are briefly described.

Chapter III gives an overview of the FEL components and of the Continuous Electron Beam Accelerator Facility (CEBAF), and basic principles of FEL theory. In Chapter IV, the CEBAF/National Institute of Science and Technology (NIST) wiggler is discussed.

Chapter V summarizes the theory of the pulsed wire method for wiggler magnetic field error measurement. This method provides accurate determination of the magnitude and location of magnetic field errors in the wiggler, and can be done in near real-time and with higher resolution than the conventional Hall probe technique. The CEBAF/NIST wiggler was measured at CEBAF using this method.

Chapter VI describes the equipment and methods of the pulsed wire experiment. The pulsed wire experiment and magnetic field error measurement of the CEBAF/NIST wiggler were presented at the 14th International Free Electron Laser Conference, which was held in Kobe, Japan from 23-28 August 1992 [9]. A paper entitled "Magnetic Field Error Measurement of the CEBAF (NIST) Wiggler Using the Pulsed Wire Method" [10], has been submitted to *Nuclear Instruments and Methods in Physics Research* for publication.

II. MOTIVATION FOR THE SHIPBOARD FREE ELECTRON LASER

A. THE CURRENT THREAT

While superpowers have long had cruise and ballistic missile capability, many third-world nations are now able to launch cruise or ballistic missiles at targets close to their territorial homelands, including U.S. forces or interests. This provides a serious threat to those forces, and requires a substantial commitment of assets to counter these weapons. Unfortunately, while current defensive weapon technology may be sufficient to counteract most cruise missiles, especially those now widely held by third-world nations, theater ballistic missile defense (TBMD) technology lags far behind.

B. CRUISE MISSILES

New generation cruise missiles are becoming a greater threat for the fleet because of their high speed and maneuverability. These abilities stretch the ability of defensive systems to cope with quick reaction targets, especially in a multiple missile raid. As an example, the Aerospatiale/MBB Supersonic Anti-Ship Missile (ANS) flies at approximately 30 ft at 2+ Mach (M) and is capable of 10 g terminal jinking maneuvers to confuse defenses [11]. This missile will possibly see active service in 1994. As a rule of thumb, defensive missiles require approximately three times the maneuverability of the offensive missile. Even if a defensive missile capable of 30 g maneuvers were developed, the same technology could easily be used to create an cruise missile, thereby negating the defensive missile. Ships employing a vertical launch system (VLS) can notice an additional problem; when the defensive missile leaves the VLS cell, it will immediately tip over and "skid" while accelerating and maneuvering to engage the target. This type of flight profile takes more time for engagement than for a missile launched from a standard

missile launching rail, which is aimed to allow for a ballistic intercept. As cruise missile speeds increase, this time difference may be decisive in determining the ship's survival. If a high speed cruise missile is not picked up until close range, the intercept range from the ship will decrease dramatically.

High diving cruise missiles can also pose a problem. Older air search radars are effectively blind at high elevation angles, and will therefore not see missiles diving within this cone. Even if the missile is destroyed, fragments will continue to fall on a ballistic path, and some may strike the ship and damage topside electronic gear, effectively giving the cruise missile a "soft" kill. Missiles such as the Soviet AS-6 Kingfish air-to-surface cruise missile, which is capable of high altitude cruise at 3 M and a steep dive onto the target, are typical of the current threat.

Other defensive measures against cruise missiles are becoming less effective. The use of radar decoys and chaff no longer has a high probability of success against modern radar-guided cruise missiles. Similarly, flares are also ineffective against modern infrared tracking missiles. Electronic counter measures are still a potent method of defense, but are not as assured as a hard kill by a defensive missile. Laser systems designed to counter electro-optically guided missiles are in development [12]. Close-in weapons systems are only effective out to approximately one thousand yards and can subject the ship to damage from ballistic fragments and a possible soft kill. These weapons are only used as a last-ditch effort.

Another concern is the recent proliferation of former Soviet weapons to the third-world. States of the former Soviet Union are in need of hard currency, and are willing to sell equipment previously only available internally. The recent sale of Tu-22M Backfire bombers, presumably with their normal armament, the AS-6 Kingfish missile, along with An-72 maritime reconnaissance aircraft, and MiG-29 and MiG-31 fighters to Iran [13]

typify the problem. This sale is particularly disquieting since the range of the AS-6 will allow Iran to launch missiles at targets throughout the Arabian Gulf from well inside Iranian territory. Also, the sale of the incomplete Russian large-deck aircraft carrier *Varyag* and Su-27K carrier aircraft to China, and of *Kilo* class submarines to Iran further exemplify this problem [10].

C. BALLISTIC MISSILES

The recent war in the Arabian Gulf and the resulting use of ballistic missiles (BMs) highlight some other problems facing defensive forces. Ballistic missiles can have very high terminal speeds of approximately 5 to 7 M, and can have steep dive angles of greater than 50°. An anti-ballistic missile (ABM) will ideally be launched so the engagement will occur at a sufficient altitude for re-engagement if needed. Assuming a BM speed of 5 M and a ABM speed of 4 M, the ballistic missile must be engaged at a slant range of approximately 135 km for an intercept at 60 km (~ 66 kyd), since the defensive missile requires approximately 50 seconds for intercept. If a second shot is required, it will intercept at only approximately 27 km (~ 30 kyd) assuming instant battle damage assessment (BDA). The intercept range will be shorter for a longer BDA time. Defensive missiles for this type of engagement will have to have extremely fast fuzes and blast action, since the closure speed is approximately 9 M.

In this type of situation, the ABMs will typically be fired as a two shot salvo, with each missile separated by a short time. If needed, a third ABM might be fired if enough time remains before ballistic missile impact. This type of scenario (shoot-shoot-look-shoot) will give a higher probability of kill (P_k) than for a shoot-look-shoot scenario, although it expends twice as many rounds and can quickly lead to magazine depletion.

Even with a successful engagement, the debris from the BM, including an unexploded warhead or liquid fuel cells, can still cause extensive damage on the ground. Although

damage from exploding debris is not as critical for tactical defense, since most tactical targets are at least somewhat protected against a near miss, civilian population centers are not as fortunate. This problem is even more complicated when nuclear, biological or chemical warheads are carried. These missiles must be destroyed far away from population centers to allow the missile fragments to burn up during re-entry into the earth's atmosphere, or for chemical or biological agents to disperse in the atmosphere to non-lethal levels.

Several countries have been actively pursuing nuclear weapons programs, such as Iraq and North Korea [14], with the intent of modifying current ballistic missiles or building new missiles to form a nuclear ballistic missile force.

The use of a single defensive missile to defend against both cruise and ballistic missiles will be a difficult task. The physical size of a ship's missile magazine is limited, and cannot hold a sufficient number of missiles of different types to adequately defend against both types of missiles. Clearly, a better solution is needed; one with the ability to successfully engage all incoming missile threats and capable of repeated engagements over an extended period. A speed-of-light weapon will fit this requirement.

D. WHY A LASER?

A high energy laser (HEL) can effectively counter high speed and quick reaction targets since light travels much faster than all other weapons. Using the example from above, a laser would require only 200 μs to reach the ballistic missile, and would only require approximately one second of dwell time to destroy the target.

E. CURRENT LASER SYSTEMS

1. The MIRACL Laser

Several laser systems have been proposed to defend against the future missile threat. The Navy's Mid Infrared Advanced Chemical Laser (MIRACL), at White Sands Missile Range, is a deuterium fluoride (DF) laser with a laser output of 3.8 μm [8], which is within the optimized atmospheric propagation range. This laser system burns NF_2 and D_2 to produce excited DF (DF^*), which is forced through the resonant cavity at high speed and radiates to produce the laser output.

In a presentation by Dr. Robert S. Bradford, Manager, Directed Energy Systems, Applied Technology Division, TRW Space & Technology Group, to the Naval Postgraduate School [8], a proposed shipboard laser system was discussed. This discussion focused placing a High Energy Laser Weapon System (HELWEPS) onboard on a *Ticonderoga* (CG-47) class guided missile cruiser, replacing the forward 5"/54 Mk 45 gun mount with a laser based on MIRACL components.

All of the HELWEPS components would fit into the deck and below decks spaces now occupied by the forward 5"/54 Mk 45 gun. The beam director, and jet engine intake and exhaust are located on the main deck, with all other equipment below decks. The jet engines are used to force the DF through the resonant cavity and to exhaust the toxic gases into the atmosphere. The gas stowage tanks are accessible through deck hatches, and can be replaced at sea during an underway replenishment (UNREP).

Although HELWEPS is an untried system, the MIRACL laser has been lasing for several years at weapons grade power levels (> 1 MW) and has been used to destroy test targets of various types and flight profiles. However, several drawbacks to the use of a chemical laser remain. First, the magazine depth, while extensive, is limited by the amount of gas carried. If independently steaming or operating in a high threat environment, an

UNREP to replenish the gas supply may not be possible and the magazine may become depleted. Second, the output is not tunable, which can limit the laser performance when operated in imperfect atmospheric conditions, such as in high humidity or a high aerosol environment. Third, the chemicals are highly toxic and reactive. This requires special handling and storing of chemical tanks. The exhaust gases are also highly toxic, and exhaust gas venting systems are needed to safely remove the gas from areas where they can be ingested by exposed personnel. Also, since the DF is transported through the resonator at high speed, line broadening of the laser output will occur which will degrade long-range performance.

2. The Free Electron Laser

Another laser design is the Free Electron Laser (FEL), which has been chosen by the Strategic Defense Initiative Office (SDIO) for future TBMD, and is a candidate for use as a shipboard FEL (SFEL). This laser uses relativistically accelerated electrons as the active medium. The FEL has several advantages over chemical lasers. First, the magazine depth is unlimited since the active medium contains only electrons. This will enable the ship to fight continuously, without requiring to UNREP for missiles or chemical laser gases. Second, the output is tunable over a broad range of wavelengths. This can be accomplished since $\lambda \propto \gamma^2$, where λ is the laser output wavelength and γ is the electron beam Lorentz factor. FELs have demonstrated output from the infrared (IR) to the deep ultraviolet (DUV). This means the FEL output can be tuned according to current atmospheric conditions and optimized for maximum effective range. The limiting factor of the FEL output tunability is the resonator optics, which typically have narrow transmission bandwidths, especially in high power laser systems. Unlike the chemical laser, the byproducts of the FEL are easily managed using energy recovery or standard beam dumping techniques.

There are, however, drawbacks to use of a FEL. First, the technology is not yet mature. While current FELs have demonstrated very high peak powers on the order of a GW [15, 16], the average power is low, on the order of 10 W [17]. Although weapons class FELs do not currently exist, electron accelerators such as CEBAF which incorporate superconducting technology show promise for high average power operation at high efficiencies [18]. Second, the ship must essentially be designed around the electron accelerator, which negates conversion of a current combatant vessel to carry a SFEL, and greatly increases the initial cost of putting this weapon at sea. Also, the FEL will require an extreme amount of power to lase. If an output of 2 MW is assumed with a wallplug efficiency of 25 %, the FEL will require 8 MW of power. This would probably require the use an electric drive system such as the integrated electric drive (IED). This propulsion system is still under study.

F. LASER EMPLOYMENT

A shipboard laser system, whether HELWEPS or SFEL, will be employed using roughly the same tactics as for defensive missiles. As a target is detected, it will be prioritized and scheduled for engagement by the ship's fire control system. The detection can be made by the ship's organic sensors, or off-board sensors such as another ship, an aircraft or national assets. The SPY-1 radar system has proven capabilities against sea skimming and high diving cruise missiles, and may have promise for ballistic missile detection capability. At the appropriate time, the laser beam director will lock onto the target and begin lasing. The missile will typically require about one second of lasing for destruction. Once BDA is completed, the target can be re-engaged if necessary, or dropped from the system, and the laser designated to the target with the next highest priority.

Typical firing ranges for sea-skimming targets are 3 - 5 km (3.3 - 5.5 kyd) and approximately 20 km (~ 22 kyd) for high altitude targets.

III. THE FREE ELECTRON LASER

A. FREE ELECTRON LASER COMPONENTS

An FEL oscillator consists of three major components; the electron accelerator, the undulator and the resonant cavity (Figure 1). An electron accelerator provides a relativistic electron beam, usually pulsed, which then passes through the undulator. The undulator causes the electron beam to undergo a periodic acceleration, which results in spontaneous radiation. The spontaneous radiation stored in the resonator and the electron beam will couple and lead to stimulated emission, which is captured and outcoupled in a resonator of standard design.

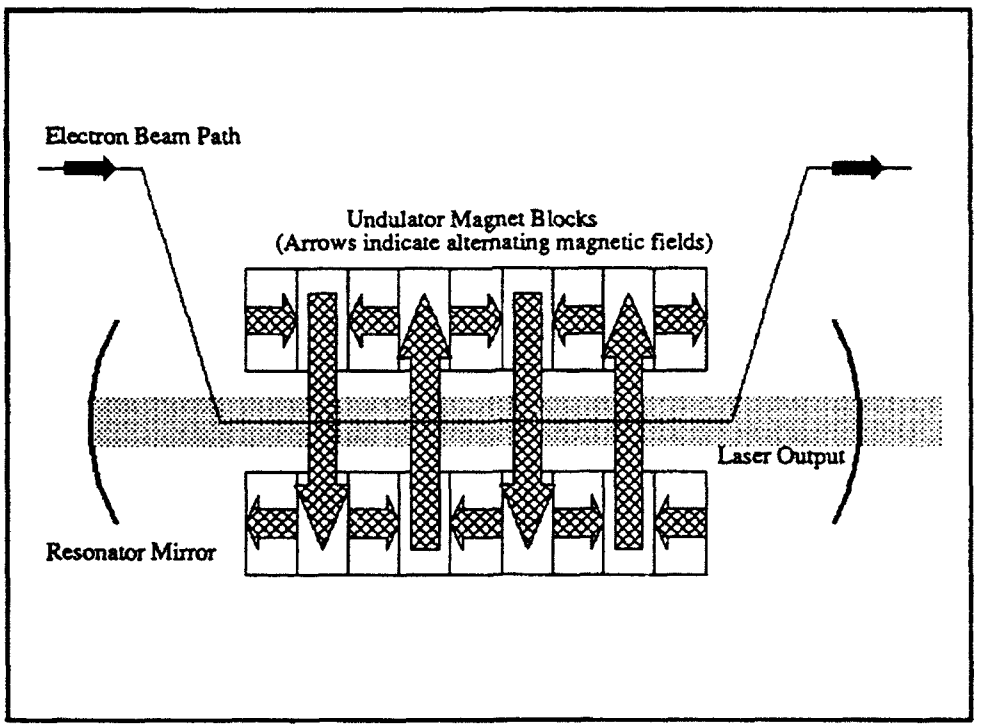

Figure 1 - FEL Schematic Showing Major Components.

Many accelerators are of the radio frequency (RF) design. This type of accelerator is capable of producing pulses as short as a few picoseconds and peak currents as high as hundreds of Amperes.

Undulators are of three basic magnet configurations: Permanent magnet undulators, electro-magnet undulators, and hybrid undulators. Hybrid undulators use permanent magnets with metallic pole pieces to concentrate the magnetic flux. In all three types, the magnetic fields alternate vertically upward and downward in a periodic manner. The undulator is typically constructed [19] with $N \approx 100$ periods, each with a wavelength, λ_o, of a few centimeters, making the undulator on the order of a few meters long. The undulator can be characterized by its undulator parameter, K, given by $K = e\overline{B}\lambda_o / 2\pi mc^2$, where e is the magnitude of the electron charge, $\overline{B}$ is the rms magnetic field along the undulator axis, m is the electron mass, and c is the speed of light in vacuum. Typically, $K \approx 1$. The undulator will cause the electrons to emit radiation with wavelength given by $\lambda = \lambda_o(1+K^2)/2\gamma^2$, where γ is the Lorentz factor of the electron beam.

B. CEBAF OVERVIEW

The Continuous Electron Beam Accelerator Facility (CEBAF), under construction in Newport News, Virginia (Figure 2), contains a superconducting, recirculating, continuous wave (CW) linac that will provide nominal 4 GeV, 200 μA electron beams simultaneously to nuclear physics experiments in three end stations [18]. A facility for high average power IR and UV FELs has been proposed. The proposed FELs would be integrally linked to and operated in parallel with the CEBAF superconducting accelerator, which incorporates two 400 MeV linear accelerators (linacs) interconnected by recirculation beamlines to provide simultaneous electron beams at energies from 800 MeV to 4 GeV for nuclear physics experiments in three end stations. FEL operation would be substantially transparent to the nuclear physics program.

The IR FEL will use the 45 MeV injector, and will produce an average power of approximately 1 kW at wavelengths from λ = 4.5 to 20 μm. The UV FEL will use the 400 MeV from the north linac, and will provide wavelengths from λ = 150 to 260 nm at an average power one the order of a kW. CEBAF parameters are given in Table 1.

TABLE 1 - CEBAF ACCELERATOR PARAMETERS

	IR FEL	UV FEL
Electron Kinetic Energy (E_e)	45 MeV	400 MeV
Lorentz Factor (γ)	87.8	780.6
Energy Spread ($\Delta E/E$)	$2 \cdot 10^{-3}$	$2 \cdot 10^{-3}$
Electron Beam Radius (r_e)	370 μm	370 μm
Pulse Repetition Frequency	7.485 MHz	7.485 MHz
Charge/Bunch	120 pC	120 pC
Momentum Spread	2×10^{-3}	2×10^{-3}
Bunch Length	2 ps	2 ps
Peak Current	60 A	120 A
Normalized Emittance (ε_n)	15 mm·mrad	15 mm·mrad

C. BASIC PRINCIPLES

The basic principle behind the operation of an FEL is the transfer of energy from the electron beam to the electromagnetic wave. As the electrons travel through the undulator, they are accelerated and radiate photons into a forward cone. Some of the radiation will be captured by the laser resonator, and be reflected and returned to the undulator. The optical radiation can couple with the accelerating electron beam and lead to stimulated emission and coherent radiation. The amplitude, period and uniformity of the electron oscillations determine the quality and quantity of light produced.

The electron trajectories in the absence of an optical field are determined by the Lorentz force equations of motion [20],

$$\frac{d\bar{\beta}_\perp}{dt} = -\frac{e}{\gamma mc}\left(\bar{\beta} \times \bar{B}\right)_\perp, \quad \dot{\gamma} = 0, \quad \gamma^{-2} = 1 - \beta_z^2 - \beta_\perp^2, \tag{1}$$

where $\bar{\beta}c$ is the electron velocity, $\bar{\beta}_\perp c = (\beta_x, \ \beta_y, \ 0)$ is the transverse electron velocity and $\bar{B}$ is the undulator magnetic field. In an ideal helical undulator, the magnetic field near the wiggler axis is given by, $\bar{B}_h = B[\sin(k_o z), \ \cos(k_o z), \ 0]$, for $0 < z < L$, where

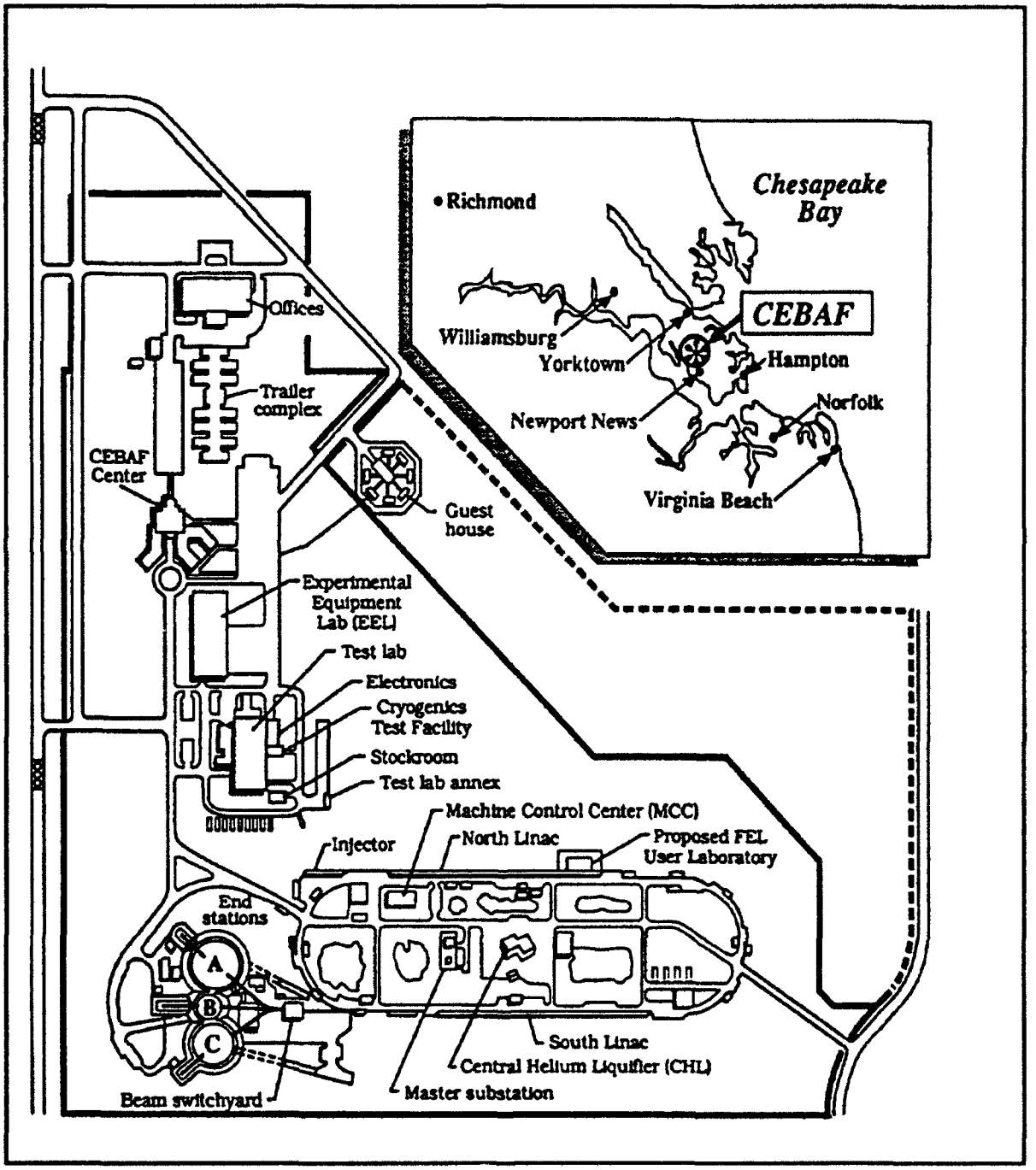

Figure 2- CEBAF Site Plan.

$k_o = 2\pi/\lambda_o$ is the undulator wave number. With perfect injection, the Lorentz force equations can be solved exactly to describe ideal orbits,

$$\bar{\beta}_\perp = -\frac{K}{\gamma}[\cos(k_o z), \quad \sin(k_o z), \quad 0], \tag{2}$$

where $\bar{\beta}_\perp c$ is the transverse electron velocity. Using the relations given in equations (1),

$$\beta_z^2 = 1 - \frac{1+K^2}{\gamma^2}, \tag{3}$$

which shows that the velocity component along the undulator axis is independent of z. Assuming perfect injection, equation (1) can be integrated further to get,

$$\bar{r}_h(t) = \left[-\frac{K\lambda_o}{2\pi\gamma}\sin(\beta_z\omega_o t), \quad \frac{K\lambda_o}{2\pi\gamma}\cos(\beta_z\omega_o t), \quad \beta_z ct\right], \tag{4}$$

where $\bar{\beta}_z \approx 1-(1+K^2)/2\gamma^2 \approx 1$ is the average z-velocity and $\omega_o = ck_o$ is the undulator frequency. Typical undulator parameters of λ_o = 3 cm, N = 100, K = 1 and γ = 100 give a transverse oscillation amplitude of $K\lambda_o/2\pi\gamma \approx 50\mu m$.

For a linear undulator with an ideal magnetic field near the undulator axis given by, $\bar{B}_l = [0, \quad B\sin(k_o z), \quad 0]$, we have [19],

$$\beta_z^2 = 1 - \frac{2K^2\cos(2k_o z)+1}{\gamma^2}, \tag{5}$$

which shows that the electron z-velocity depends on z, even for a perfectly injected electron beam. For typical undulator parameters of, K = 1 and γ = 100, $K/\gamma << 1$. The resulting electron trajectory is,

$$\bar{r}_l(t) = \left[-\frac{K\lambda_o}{\sqrt{2}\pi\gamma}\sin(\omega_o t), \quad 0, \quad \bar{\beta}_z^2 ct + \frac{K^2\lambda_o}{8\pi\gamma^2}\cos(2\omega_o t)\right], \tag{6}$$

where $\bar{\beta}_z \approx 1-(1+K^2)/2\gamma^2 \approx 1$ is the average velocity.

For the CEBAF/NIST IR FEL described in Table 1, the oscillation amplitude will be $K\lambda_o/\sqrt{2}\pi\gamma \approx 71$ μm, where K = 0.99 is the undulator parameter, λ_o = 2.8 cm is the undulator wavelength, and γ = 87.8 is the electron beam Lorentz factor. The oscillation amplitude is much less than the electron beam radius of 370 μm. Similarly, the oscillation amplitude for the CEBAF/NIST UV FEL is, $K\lambda_o/\sqrt{2}\pi\gamma \approx 11$ μm, where K = 1.4, and γ = 781, is also much less than the electron beam radius of 370 μm. Equation (6) shows that the electrons oscillate twice as fast in the z-direction as in the x-direction, which is responsible for radiation in the odd harmonics [21]. The electron beam also undergoes betatron oscillations, which are slow transverse oscillations superimposed onto the motion described in equation (5), and have a wavelength of, $\lambda_\beta = \lambda_o\gamma/2\pi K$. These oscillations are characteristic of the natural focusing of the wiggler, and are important when $\lambda_\beta \le L$. For the CEBAF/NIST IR wiggler, λ_β = 0.394 m << L = 1.5 m, which indicates that the NIST wiggler would be strongly focusing if used with the CEBAF accelerator as an IR FEL. For the CEBAF/NIST UV wiggler, λ_β = 2.46 m, which also indicates that the wiggler will not be strongly focusing.

The gain of the laser can be calculated from the average energy change of the electron beam. For a single electron, the change is given by, $\dot{\gamma} = -e(\bar{\beta}\cdot\bar{E}_r)/mc$, where $\bar{E}_r = E[\cos(kz-\omega t+\phi),\ -\sin(kz-\omega t+\phi),\ 0]$. Using $\bar{E}_r$ and equation (4), the energy change is,

$$\frac{\dot{\gamma}}{\gamma} = \frac{eEK}{\gamma^2 mc}\cos(\zeta+\varphi), \tag{7}$$

where $\zeta(t) = (k-k_o)z(t)-\omega t$ is defined as the electron phase, where $k = 2\pi/\lambda$ is the optical wavenumber, and relates the positions of the electrons and the optical wave. Notice from equation (7) that the electron will gain energy from the optical field if $-\pi/2 <$

$(\zeta+\varphi) < \pi/2$, and will lose energy to the electron beam if $\pi/2 < (\zeta+\varphi) < 3\pi/2$. If the beam becomes bunched at phase $\pi/2 < (\zeta+\varphi) < 3\pi/2$, then the FEL beam will give up energy to the optical wave.

It is often desirable to relate the various equations to dimensionless parameters to allow different FEL configurations to be easily compared. Define $\tau = ct/L$ as the dimensionless time, so that the electrons travel from $z = 0$ to L as they evolve from $\tau = 0$ to 1. The electron phase velocity is then defined as,

$$\upsilon(\tau) = L\left[(k+k_o)\beta_z - k\right] = d\zeta/d\tau, \tag{8}$$

with the dimensionless pendulum equation,

$$\frac{d\upsilon(\tau)}{d\tau} = |a|\cos(\zeta+\varphi), \tag{9}$$

where $|a| = 4\pi NeEKL/\gamma_o^2 mc^2$ is the dimensionless optical field amplitude.

Other dimensionless parameters include the Rayleigh length, $z_o = Z_o/L$, the normalized mode waist radius, $w_o = \sqrt{z_o}$ and the slippage distance, $\Delta s = N\lambda$. The slippage distance is the distance that the optical mode and the electron beam remain in contact down the undulator and can therefore exchange energy.

When $\upsilon(\tau) = 0$, we have, $k = k_o\beta_z/(1-\beta_z)$, so that the electron beam and the optical mode are in resonance. Since $\beta_z \approx 1-(1-K^2)/2\gamma^2 \approx 1$ assuming $\gamma >> 1$, the resonant wavelength, λ, is given by,

$$\lambda = \lambda_o \frac{1+K^2}{2\gamma^2}. \tag{10}$$

As the electrons enter the undulator, they oscillate in response to the periodic magnetic field, and spontaneously radiate photons into a forward cone of instantaneous width $\sim 1/\gamma$. Some of this radiation is captured in the resonator and circulates through the cavity, stimulating other electrons to emit photons. The electrons are, however, equally good at absorbing the light energy as releasing it. During laser start-up, emission and

absorption occur at approximately the same rate, but a small range in wavelengths have a net gain, resulting in a self-sustaining optical mode.

As mentioned above, undulators are constructed by alternating pairs of magnets with opposite magnetic moments (Figure 1). In hybrid wiggler designs, such as the CEBAF/NIST wiggler, metal pole pieces are used to concentrate the magnetic flux in the vertical direction (y-direction). Unfortunately, even with the most careful manufacturing techniques, the magnetic moments of the magnets do not have the exact same orientation and magnitude. Figure 3 shows details of the magnetic field taken by a Hall probe in a portion of the wiggler. Note that the period-to-period variation is on the order of a few percent, and includes errors from both the Hall probe measurement as well as those from the wiggler. These variations introduce errors in the phase and path of the electrons as they travel down the undulator axis. At best, the errors can lead to a slight degradation of gain. At worst, the electron beam can wander completely outside the optical mode, leading to zero gain in that region or even burn through the beam transport tube.

Undulator construction normally contains four steps: measuring the individual magnets, assembling the undulator, testing the undulator, and adjusting to correct for "bad" magnets [22]. The individual magnets are tested separately, and then paired with another magnet of approximately equal parameters to form one half-period segments. To correct for anomalies, each half-period magnet set is normally matched with a magnet set of opposite polarity with appropriate characteristics to compensate for the imperfect field components. Elaborate computer codes exist to optimize this task [23]. Once the undulator is assembled, magnetic field measurements are usually made with a Hall probe. This method is tedious because of the large number of measurements required to fully characterize the wiggler and the great time involved. A larger Hall probe chip would speed up the measurements, but accuracy would suffer since the chip averages over a

larger area. Even small Hall probe chips are several times larger than the electron beam, so the field sampled by the probe is not the same as the field seen by the electrons. Also, once the undulator is installed in its final site with the electron beam transport vacuum tube and ancillary equipment, it is in a very different environment than in which it was tested. This environment change can cause additional errors in the undulator magnetic field, further degrading the FEL performance. Many pumps and other new magnetic sources are present, requiring additional magnetic mapping to fully describe the wiggler in its permanent location. Smaller errors include changes in magnetic moment caused by thermal and radiation effects [23]. The use of a Hall probe once the wiggler is installed is further complicated due to the vacuum line obstructing the wiggler axis.

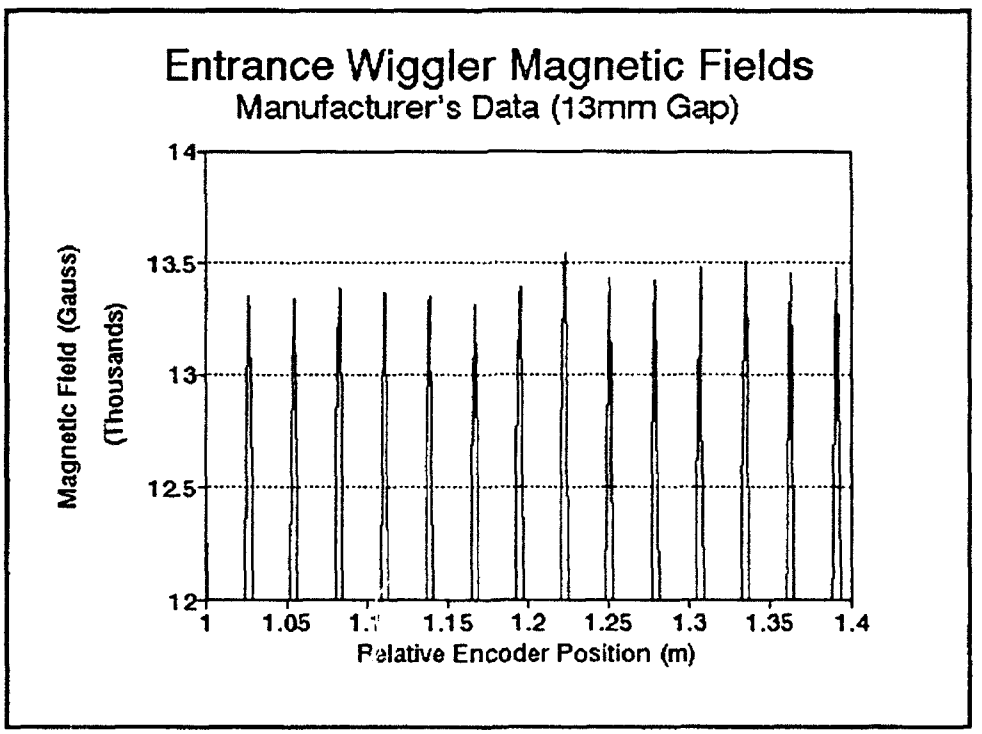

Figure 3 - Details of the Magnetic Field Map From the Manufacturer's Hall Probe Data.

IV. THE WIGGLER

The CEBAF/NIST wiggler is a 130 period linearly polarized hybrid wiggler constructed in two 65-period halves. The magnetic gap is variable over the wiggler length and can be adjusted to obtain either a constant or tapered gap as desired. The undulator halves are designed to be mounted on a common base anchored to the floor for ease of vertical and horizontal alignment (Figure 4). At the entrance and exit of each section are electromagnetic correction coils designed to provide a magnetic field of half nominal strength. Without this initial "half-period kick", the electrons will enter the first period of the undulator and be deflected, causing the electrons to eventually wander out of the optical mode. With the kick, the electrons will experience sinusoidal motion centered on the wiggler bore. The electron beam path in Figure 5 is rotated 90° with respect to the wiggler axis to make it visible. The center of each half also has an electromagnetic steering element to correct for horizontal angular trajectory errors. The wigglers are mechanically independent and can be operated with the full 130 periods at a constant or smoothly tapered gap, or with the exit-half magnetic gap widened so that the fields are negligible. For the CEBAF IR FEL, only the entrance wiggler half will be used, with a constant magnet gap of 13 mm and a corresponding field amplitude of 0.38 T. For the CEBAF UV FEL, the full wiggler will be used, with a constant magnet gap of 10 mm and a corresponding field amplitude of 0.54 T. The wiggler manufacturer's parameters are included in Table 2. For additional details of the NIST FEL proposal, see reference [23]

The wiggler gap and entrance/exit electromagnet correction coil currents were controlled by a computer located in an equipment rack along with the correction coil power supplies, gap sensor monitors and Hall probe equipment. The desired wiggler gap was set manually in the computer, which then adjusted the gap and set brakes to prevent

further movement. Gap reproducibility was ± 25 μm. Correction coil currents were also set manually in the computer, which set the correction coil power supplies. Input information was sent to the instruments via digital to analog (D/A) conversion with feedback information returned to the computer via analog to digital (A/D) conversion.

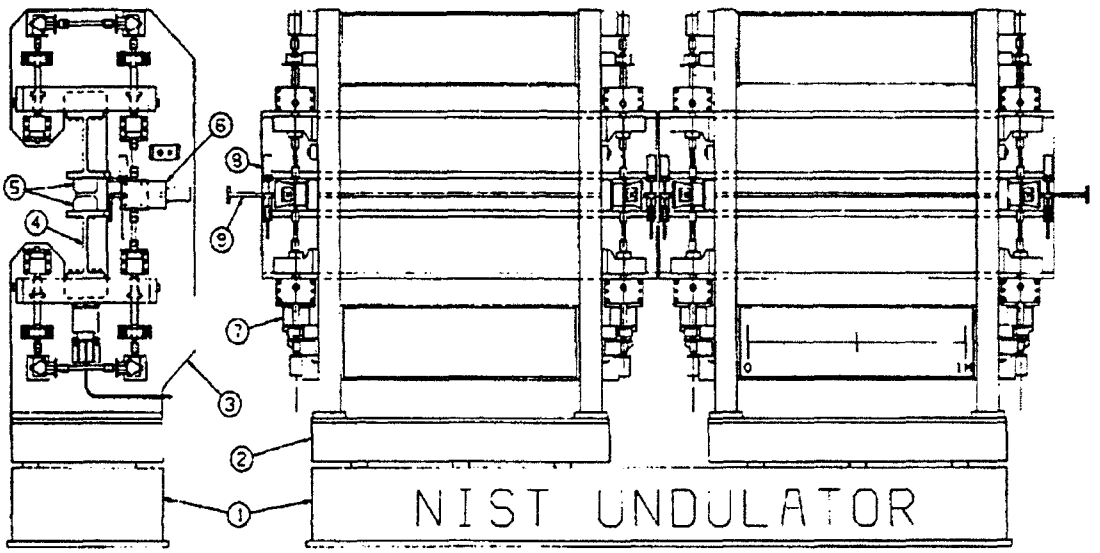

1. Sub Base
2. Half Wiggler Base
3. Aluminum C-frame
4. Steel I-beam
5. Magnet Assemblies
6. Gap Adjustment Mechanism
7. Air Springs
8. Gap Opening Sensor
9. Vacuum Chamber

Figure 4 - Wiggler Diagram Showing Major Components.

The wiggler was received with the Hall probe used by the manufacturer to map the magnetic fields, and the resulting magnetic maps. The Hall probe was mounted on a 1 m long motorized precision stage with adjustment in the x- and y-directions. A linear encoder was used to send position data to the wiggler control computer. Since the motorized Hall probe stage was shorter than the 3.6 m wiggler, four overlapping map runs were used for a full undulator magnetic map, with each run starting from a relative

encoder position of zero. The runs were reproducible, and could be joined by noting the encoder position where the two maps overlapped. The data files were then merged using that overlapping point as the new encoder reference point for the second map run. The manufacturer's Hall probe field maps were not verified because of equipment problems occurring in shipment.

TABLE 2 - CEBAF/NIST WIGGLER PARAMETERS

Physical Parameters	
Number of full strength periods (N)	130
Undulator period (λ_o)	28 mm
Undulator parameter (K)	
IR FEL	0.99
UV FEL	1.41
Maximum operating magnetic field (B_{max})	0.54 T
Minimum operating magnetic field (B_{min})	0.38 T
Minimum magnetic gap (G)	10.0 mm
Magnetic field shape	sinusoidal plus harmonics
Magnetic field polarization	linear
End corrector nominal strength	½ B_{max}
Maximum third harmonic field content	10 %
Field Precision	
RMS error	< 27 Gauss
Vertical field integral error	< 23 Gauss·cm
Horizontal field integral error	< 23 Gauss·cm
Magnetic Field Adjustments	
End corrector adjustment range	150 %
Integral error adjustment range	150 %
Adjustment resolution	> 10 Gauss·cm
Maximum gap taper	0.5 mm/m
Gap reproducibility	± 0.025 mm

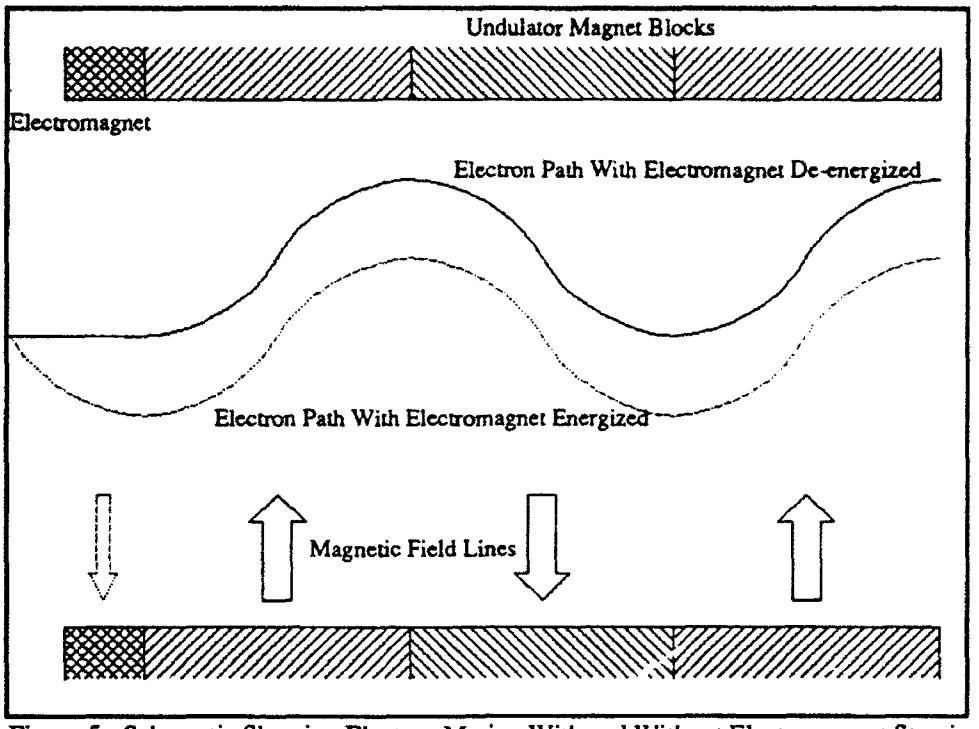

Figure 5 - Schematic Showing Electron Motion With and Without Electromagnet Steering.

V. PULSED WIRE THEORY

A new technique has been developed [24] that uses a thin wire stretched down the wiggler axis along the electron beam path. A short current pulse is then passed through the wire, which produces a force on the wire proportional to the local transverse magnetic field. This force causes periodic distortions along the wire which initiate a traveling wave that propagates in both directions. This wave is detected with a sensor package placed on the wire past the end of the undulator producing a signal which is then displayed on an oscilloscope. Since the distortions are proportional to the local transverse magnetic field, the oscilloscope trace may be studied to determine the field along the undulator.

The waveform traveling both directions along the wire can be written in the form, $x(z,t) = f(z - v_p t) + g(z + v_p t)$, where f and g are arbitrary functions, $v_p = \sqrt{T/P} \approx 312$ m/s is the phase speed of an acoustic wave on the wire, and T and P are the tension and linear density of the wire, respectively [23]. Two boundary conditions are imposed: $x(0) = 0$ when the current δ-function is applied, and $d^2x(z)/dt^2 = IB(z)/P$. The wire's displacement angle is then found to be [23]:

$$\theta_x = \frac{dx(z,t)}{c\,dt} = \frac{I\,dt}{2cv_p P}\int_o^{v_p t} B(z)dz\,, \tag{11}$$

where $dt = dz/v_p$.

The current pulse travels at virtually the speed of light, with the resulting acoustic pulse traveling ~ 300 m/s and propagating only a few mm. Consequently, if a 20 μs current pulse is used to excite the wire, the acoustic pulse will travel ~ 6 mm, or approximately $0.2\,\lambda_o$ during the pulse. A short current pulse will therefore approximate a δ-function. The signal returned from the photodetector is a measure of $x(t)$ and is, therefore, proportional to the first integral of the field versus position along the wire as

given by equation 11, and indicates the angular deflection error of the electron beam. Note that the waveform obtained from the photodetector contains information from all points in the wiggler. Only a comparison of the data values at the starting and ending points of each wiggler period — the centroid of the wire motion — contain the important data, and will give a true picture of the errors in the undulator.

Integrating the first integral from 0 to z_1 gives the second integral of the wire displacement [23]:

$$x(z) = \frac{I}{2\nu_p^2 P}\int_0^{\nu_p t}\int_0^{z_1} B(z)\,dz\,dz_1, \tag{12}$$

which is proportional to the path taken by the electron beam [23].

The electron angle and path errors can also be derived from the electron equation of motion,

$$\dot{\bar{\beta}} = -\frac{e}{\gamma mc}\left(\bar{\beta}\times\bar{B}\right). \tag{13}$$

Using the magnetic field of $\bar{B} = \left[0,\ B\sin(k_o z),\ 0\right] + \delta\bar{B}$, and assuming that $v_z \approx c >> v_x, v_y$, the electron velocity is found to be,

$$\dot{\bar{v}} = -\frac{e}{\gamma mc}\left[-c\left(B\sin(k_o z) + \delta B_y\right),\ c\delta B_x,\ 0\right], \tag{14}$$

where δB_x and δB_y are the magnetic field errors in the indicated directions. Assuming that $\delta B_x << \delta B_y \approx \delta B$,

$$\dot{\bar{v}} \approx -\frac{e}{\gamma mc}\left[-c\left(B\sin(k_o z) + \delta B\right),\ 0,\ 0\right] \tag{15}$$

Therefore,

$$\dot{v}_x = \ddot{x} \approx -\frac{eB}{\gamma m}\left(\sin(k_o z) + \frac{\delta B}{B}\right). \tag{16}$$

Integrating equation 16 from $0 \rightarrow t = \lambda_o/c$ yields,

$$v_x = \dot{x} \approx -\frac{e\delta B \lambda_o}{\gamma mc}, \tag{17}$$

which is related to the angle error by, $\Delta\theta_x \approx v_x / v_z \approx v_x / c$. Therefore,

$$\Delta\theta_x \approx -\frac{e\delta B \lambda_o}{\gamma mc^2}. \tag{18}$$

The motion described in equation (18) will cause the electron beam to experience a random deflection in an arbitrary direction from the magnetic field errors of each wiggler period. While equation (18) describes an angular deflection in only the *x*-direction, the deflection is arbitrary, and in general will also have a *y*-component. The summation of these random errors over the wiggler length results in the net deflection of the electron beam, and is known as the "random walk" of the electron beam.

Integrating equation 16 a second time results in the second integral of the electron motion,

$$\Delta x \approx -\frac{e\delta B \lambda_o^2}{\gamma mc^2}, \tag{19}$$

which is the transverse offset in the electron position over one undulator wavelength. Figure 6 shows a typical double integral measurement illustrating the electron trajectory [26].

The ability to directly evaluate the first and second integral of the wire motion is a tremendous advantage over the Hall probe technique, since the pulsed wire test only takes a few milliseconds compared to several hours for the Hall probe test. Many data samples can be taken in a short time for good statistical analysis.

There are, however, some limitations to the pulsed wire technique [23]: In a long wiggler, the wire will sag because of its own weight. If the wire is not tensioned close to

its yield strength, signal dispersion can become a problem. Acoustic noise in the ambient air also contributes to the errors.

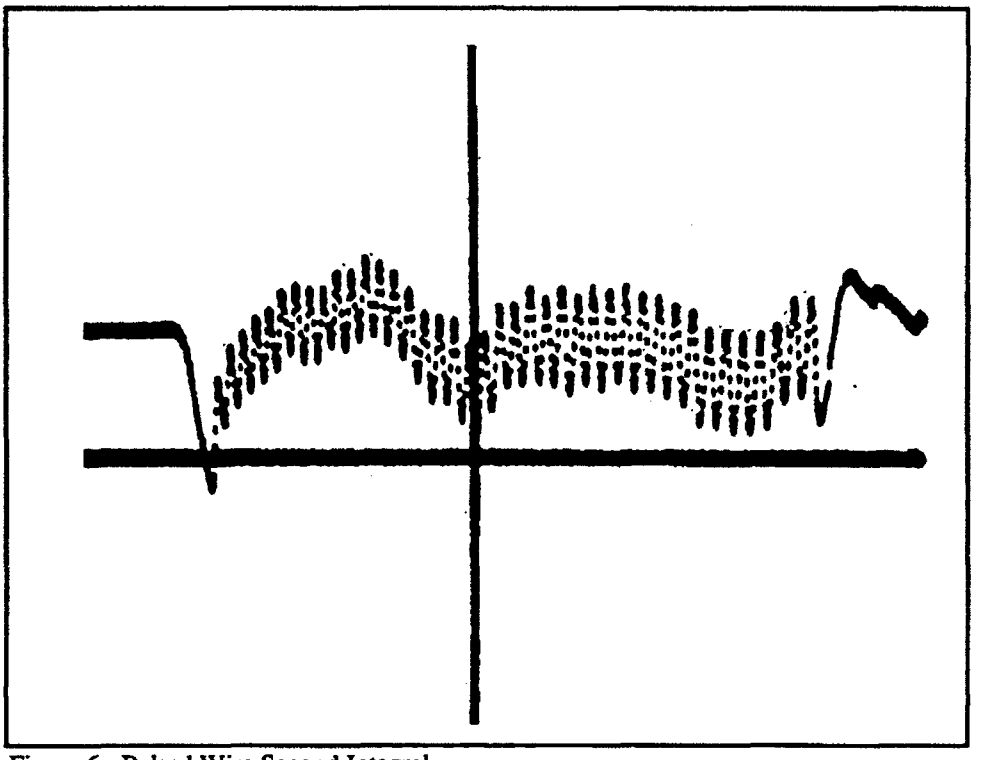

Figure 6 - Pulsed Wire Second Integral.

In a perfect wiggler, the average of each integral over an integral number of wiggler periods will be zero, corresponding to no phase or path errors. In an imperfect undulator, however, the average will not be zero. Errors can be located by noting where the slope of the integral error versus time changes. Counting the oscillation periods will indicate which magnet pairs require adjustment or replacement. Once identified, magnet errors can be fixed by shimming the magnet or the pole piece with standard machine shop shim stock and established techniques [25].

The sag in the wire can be characterized as $S = gDL^2 / 8T$, where g is the gravitational acceleration, D is the wire's volume density, $L \approx 5$ m is the wire's length and T is the

specific tension (force per unit area) [23]. The wire sag was calculated to be $S \approx 0.25$ mm. The change in magnetic field along the undulator caused by this sag is given by $\Delta B/B \approx 0.5(2\pi S/\lambda_o)^2 \approx 0.2$ %. The effect of the wire's sag can be lessened by raising up one or both of the wire support pulleys by an amount to lift the wire to the wiggler centerline at both ends of the undulator. The wire will still sag somewhat in the center of the wiggler, but will be much less than before. If a reasonable reduction of the wire gap by a factor of five is assumed, $\Delta B/B \approx 0.07$ %.

Physical methods to reduce wire sag, such a mechanical bridge, cannot be used since they would not allow the propagation of the acoustic wave to the detector. Sagging may be limited by using electromagnetic levitation of the wire [23], but is not needed in this experiment.

As the signal propagates down the wire, the shorter wavelength components travel faster than those with longer wavelengths slightly with an average speed given by $v_p = \sqrt{T/D} = 348$ m/s. This wavelength dispersion is caused by the wire's stiffness and is most pronounced when the wire is only moderately tensioned. As the tension increases near the elastic limit of the wire, the dispersion decreases until all frequencies propagate at essentially the same speed. When the signal dispersion is considered, the signal speed is given by, $v_p' = v_p(1 + aM\pi^2 d^2 / 8T\lambda_o^2) \approx 348$ m/s, where v_p is the wave speed if stiffness is ignored, $M \approx 140$ GPa is the elastic modulus of the wire, $d = 50$ μm is the wire diameter, a is a constant near unity that depends on the detailed elastic properties of the wire, and λ_o = 2.8 cm is the wiggler wavelength [23]. When the stiffness of the wire is an insignificant effect, a distortion whose wavelength is equal to the wiggler wavelength should be shifted forward much less than the wiggler wavelength is traveling to the detector. With this constraint in effect, the maximum wiggler length that can be tested is,

$L_{max} = 8T\lambda_o^3 / aM\pi^2 d^2$. For this experiment, $L < L_{max} \approx 45.5$ m, which is easily satisfied since $L \sim 5$ m.

VI. THE PULSED WIRE EXPERIMENT

A. EXPERIMENTAL SETUP

The pulsed wire method was used to measure the field errors of the entrance half at both magnet gap settings, G = 10 mm and G = 13 mm. The magnetic gap of the exit wiggler half were widened to a gap of, G ~ 160 mm. The magnetic field of the exit undulator half along the electron beam path was essentially zero, since $B \propto \exp(-\pi g/\lambda_o)$.

The wiggler halves were placed on the floor of the test area approximately one meter apart instead of being mounted on the common base. The undulator bores of each section remained aligned. This arrangement permitted the laser/photodiode assembly to fit into the area directly adjacent to the wiggler under study (Figure 7), and increased the distance to the far-end pulley to prevent reflected waves from interfering with the primary signal.

The wire was strung through the undulator over the pulleys between a fixed anchor and a hanging weight used to tension the wire, as shown in Figure 7. BeCu wire was chosen because of its low resistivity and high yield point. The low resistivity minimizes heat buildup during the current pulse, and the high yield point allows use of a very thin wire to minimize sag and cross sectional area, permitting a higher cooling rate. Since the deflection of the wire is proportional to the force applied by the magnetic field, a smaller diameter wire will undergo a greater displacement. During use, the wire was tensioned close to its breaking point to minimize dispersion of the acoustic pulse [23]. The yield strength (YS) of the BeCu wire was calculated to be 180 g using the average tensile strength of 900 MPa, and shown experimentally to be ~ 210 g. Typically, the wire is tensioned to at least 80% of YS. For this experiment, 188 g was used. See Table 3 for wire properties.

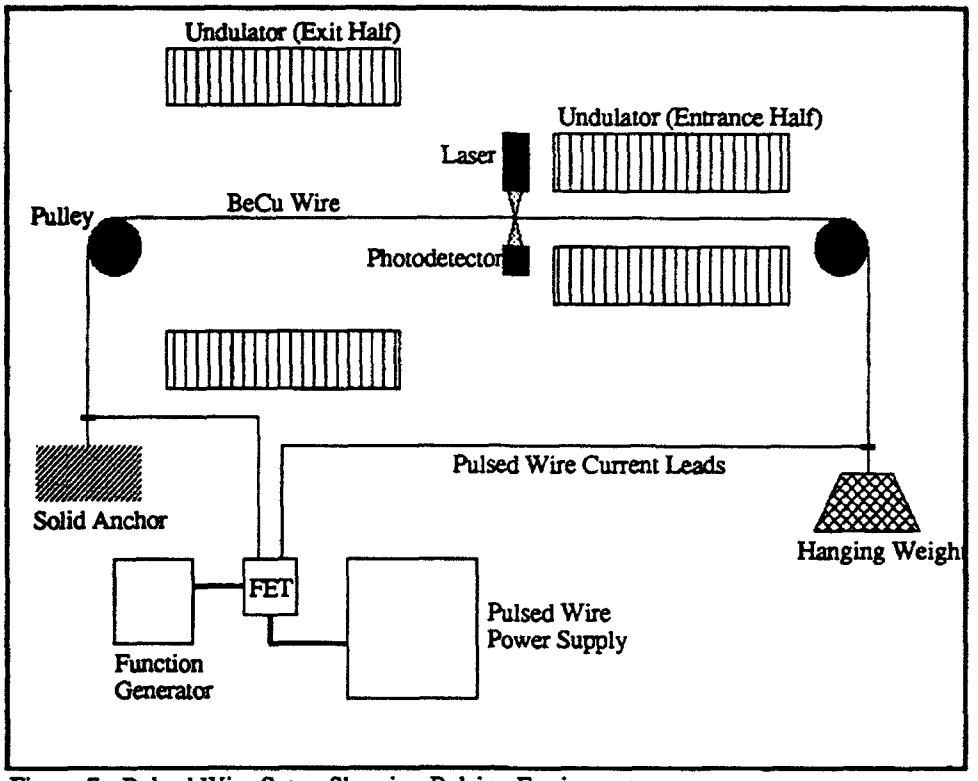

Figure 7 - Pulsed Wire Setup Showing Pulsing Equipment.

The laser/photodetector setup shown in Figure 8 was used to detect the oscillations produced in the wire by the magnetic field of the undulator. The traveling wave passes through a plate on which a semiconductor laser and photodetector are mounted orthogonal to the wire to read the signal in the y-direction. The photodetector allowed a fast response time and high resolution for the detected waves. The laser was tightly focused onto one edge of the wire with a short focal length lens, as shown in Figure 9. Figure 10 shows a Gaussian distribution typical of laser output. If the laser was focused on the center of the wire, corresponding to a small distance around the peak of the Gaussian distribution, the change in pulsed wire signal amplitude would be small and would have two maxima per wire oscillation. However, when the laser is focused on the side of the wire, corresponding to the shaded area on the right side of the peak of the

Gaussian distribution, the change in pulsed wire signal amplitude is much larger, and is approximately linear. The difference in photodetector output of a linear laser irradiance distribution and a Gaussian distribution shows that the photodetector output voltage difference will be at most a few percent. The photodetector was placed a short distance below the wire. The laser spot size was approximately 18 μm and the wire oscillation amplitude was approximately 7 μm. The laser and photodetector were mounted as a unit, and could be moved to respond to the changes in the wire's position after each wire replacement. This permitted adjustment of the laser waist position to ensure maximum signal gain when the wire was pulsed.

TABLE 3 - PULSED WIRE PROPERTIES.

Wire	
Type	BeCu (2%/98% Composition)
Diameter (d)	50 μm
Physical Properties	
Volume density (D)	8.25 g/cm^3
Melting point	860-1000 °C
Electrical Properties	
Resistivity	5.4-11.5 μΩ·cm
Temperature coefficient	0.0010-0.0018 K^{-1}
Thermal Properties	
Coefficient of expansion	17.0×10^{-6} K^{-1}
Thermal conductivity @ RTP	60-120 W m^{-1} K^{-1}
Mechanical Properties	
Brinell hardness	100-360
Elongation	< 50%
Modulus of elasticity	120-160 GPa
Tensile strength	500-1300 MPa
Weight per meter	0.01616 g

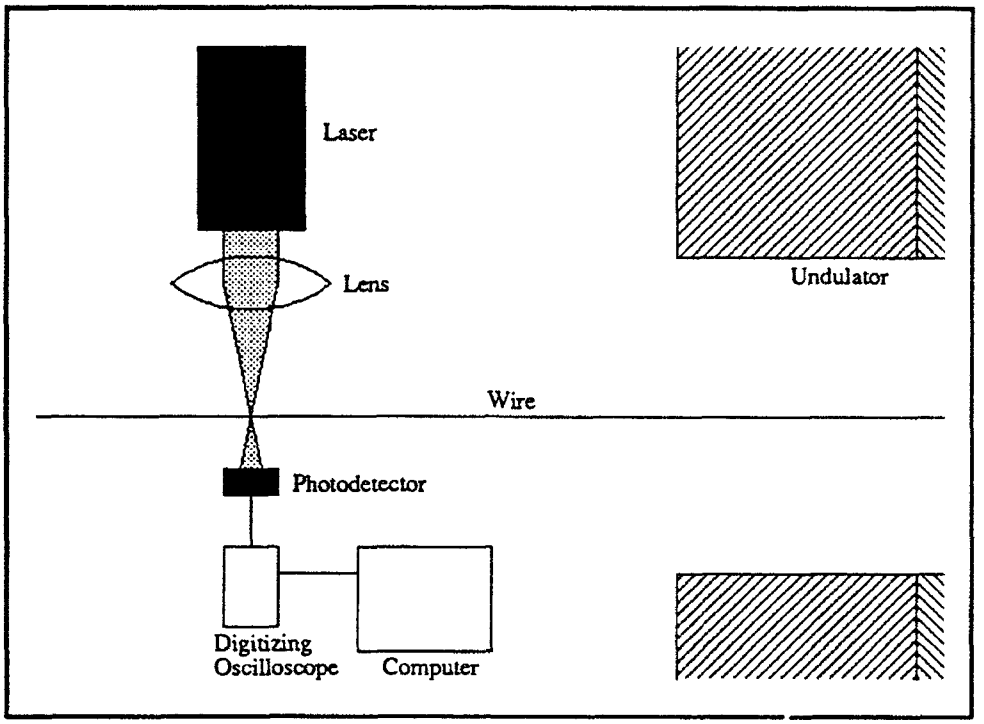

Figure 8 - Details of the Pulsed Wire Detection Equipment.

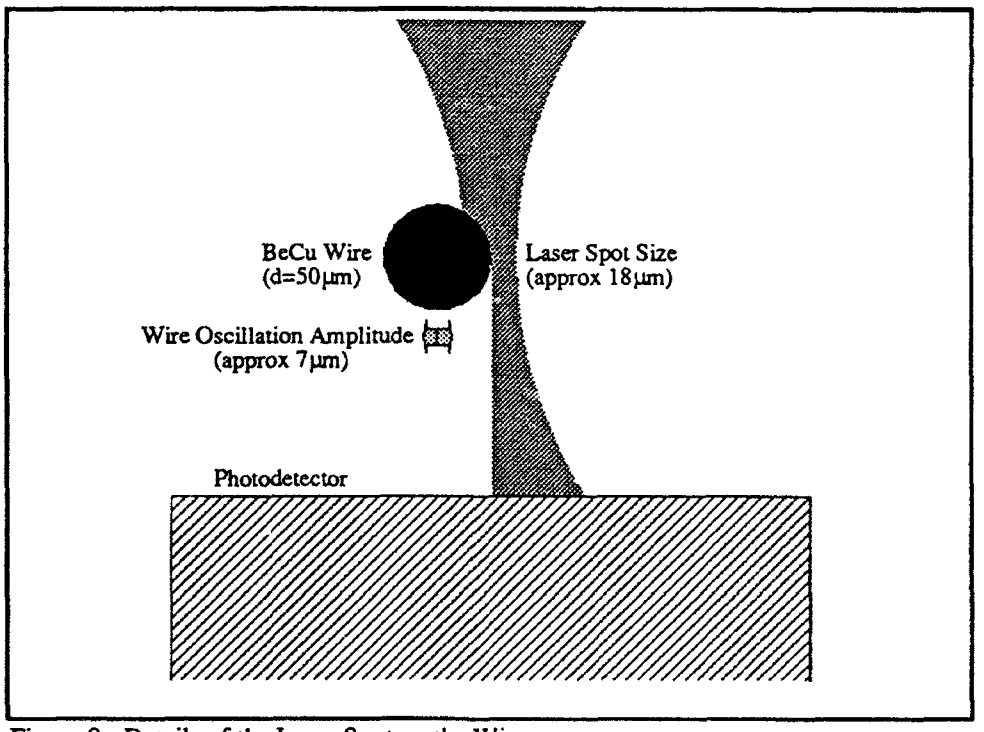

Figure 9 - Details of the Laser Spot on the Wire.

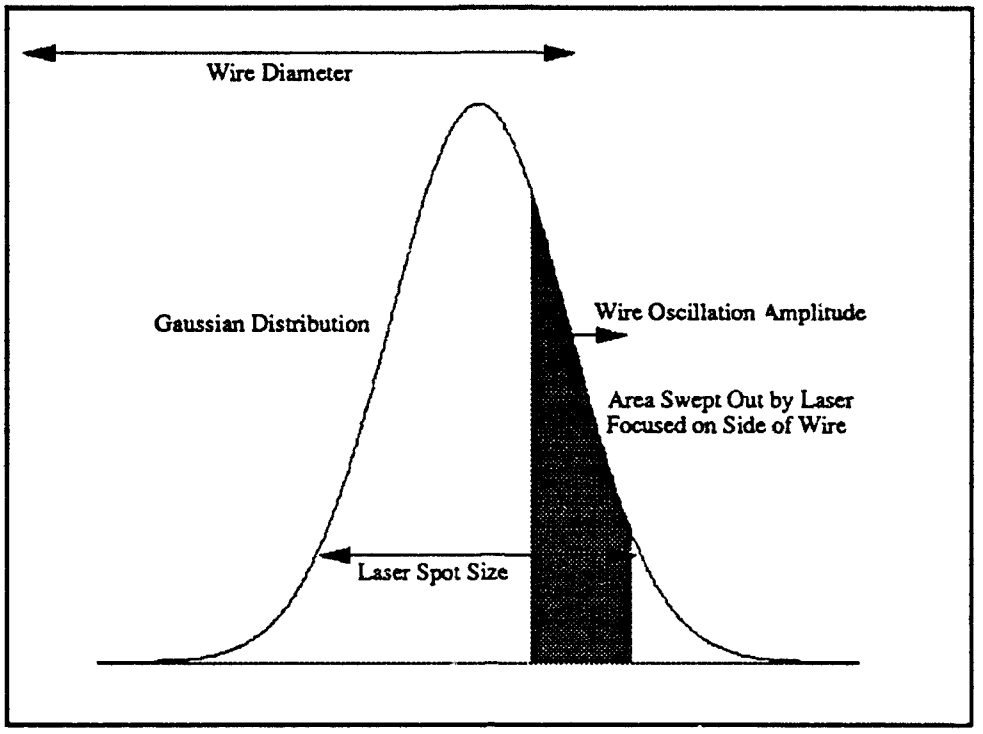

Figure 10 - Gaussian Distribution With Comparison of Laser Spot Focusing Regions.

A field effect transistor (FET) was used to transmit current to the wire. The FET was fed electrically from the pulsed wire power supply and switched by a function generator. This arrangement allowed short, high current pulses up to 2 A, with short rise-times and rapid fall-offs to provide functions approaching a δ-function. Longer pulses could be generated as required.

An inductive current pickup was used to measure the current pulse fed to the wire and was displayed on an oscilloscope simultaneously with the output signal from the function generator to the FET. The acoustic pulse signal from the photodetector was displayed on a digitizing oscilloscope and sent to a computer to convert the digital signal on a real-time basis into a spreadsheet format for later analysis. The oscilloscope was triggered by receipt of the acoustic pulse. This permitted high pulse repetition rates and

automatic data capture. The digitizing oscilloscope could also average the signal over many pulses for good statistical analysis and send the average pulse envelope to the computer.

Acoustic noise from the surrounding air could distort or even hide details of the pulsed wire signal and pose a severe problem. While the electronic signal-to-noise ratio (SNR) is ~ 100, the acoustic SNR is ~ 10 and is a more significant problem [26]. Driving the wire with a longer or larger current pulse improves the SNR, but nonlinear processes can then distort the primary signal [27]. If dirt or kinks are present on the wire, the acoustic pulse can reflect from the imperfections, and distort the primary signal. This problem can be reproduced, but will be different when the wire is replaced. Also, a longitudinal mode can propagate and interfere with the primary signal, since it is weakly coupled with the primary acoustic pulse which also stretches the wire slightly. The longitudinal signal travels much faster (~ 5000 m/s) than the acoustic pulse and can bounce between the pulsed wire supports several times while the acoustic pulse is traveling past the detector [27]. Acoustic shields were constructed to prevent the strong acoustic noise present in the testing area from masking the pulsed wire signal. The shields consisted of plywood boxes lined with styrofoam acoustic sheeting and were placed over both end stations to cover the pulleys and anchors, and in the middle to house the laser/photodiode. The wiggler bore was similarly enclosed in a cardboard and styrofoam shield. These measures were successful in reducing the air noise to an acceptable level. The pulsed wire apparatus (Figure 7 and Appendix A) was mounted to convenient locations on the wiggler halves to minimize the effects of the abundant acoustical and vibrational noise in the testing area.

B. EXPERIMENTAL PROCEDURE

The spool of BeCu wire was mounted onto the acoustic case on the exit undulator with a device providing moderate tension to permit the wire to be unreeled without kinking. The wire was then placed over the pulley and strung through the undulator bore with an aluminum knitting needle. After being placed over the pulley on the entrance end, a lead fishing weight connected to an alligator clip was clipped to a small piece of masking tape placed on the knitting needle. Great care was taken when hanging the wire. Any kinks developed while threading the wire would weaken the wire and cause it to break as soon as tension was applied. After the weight was attached, it was carefully lowered so the wire could slowly stretch and take up the tension. Lastly, the pulsed wire current leads were attached. See Figure 7.

The current pulse repetition rate was kept low (0.1 Hz) to allow the heat built up by the current pulse to dissipate and to let the acoustic pulse in the wire ring down. The laser/photodiode assembly was adjusted to obtain the maximum signal. The digitizing oscilloscope was normally used to take an average of the signal pulses, with the resulting pulse envelope sent to the computer for analysis.

As the current through the wire increased, heat buildup also increased, decreasing the number of pulses that could be passed through the wire before breaking. However, the increased current also increased the SNR, so the pulse current was set to a level providing an adequate SNR but allowed several test runs to be completed before the wire broke. Test runs were made at several current settings to find the this current value. These tests also proved that the applied force on the wire is proportional to the current and that the acoustic pulse envelopes had the same shape regardless of the current.

To get the first integral data, a 20 μs pulse was used to approximate a δ-function. Figure 11 shows typical raw first integral data. Note that the data appear in units of

Photodiode Voltage (mV) versus Time (ms). In order for this measurement to be meaningful, the ordinate had to be converted from the relative photodiode voltage to the absolute integral error. Unfortunately, this was not a simple global conversion.

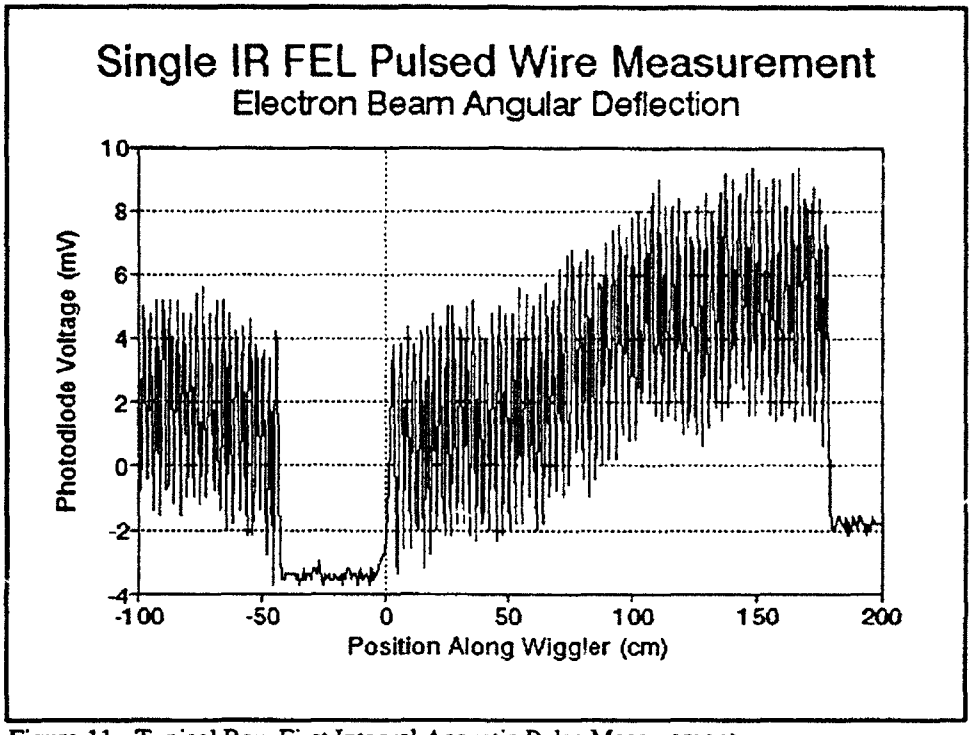

Figure 11 - Typical Raw First Integral Acoustic Pulse Measurement.

Each time the wire was strung, it would change position through the undulator bore by a few microns, requiring the laser/photodiode detector to be realigned. The laser and photodiode detector were adjusted to obtain approximately one-half the nominal voltage from the laser. This alignment was not perfectly reproducible with the different wires, and produced different oscillation amplitudes for each run. Therefore, each run required a separate normalization factor to relate the photodiode detector voltage to the integral error.

One approach to this problem is the use of a normalization wiggler [27]. This wiggler consists of several small magnets arranged to form an undulator. The magnets do not have to be of high quality or arranged to minimize errors. A Hall probe is then used to map the field of this undulator. During the pulsed wire experiment, the wire is strung through the normalization undulator which is placed in a convenient position outside of the wiggler under test. The acoustic pulse returned from the test will have unique distortions from both the normalization and test wigglers. Since the fields of the normalization wiggler are known, the resulting acoustic pulse from can be used to normalize the signal returned from the undulator under study. This is a convenient and accurate method of determining the conversion factor required to determine the wiggler's integral error. Unfortunately, Hall probes with sufficiently high resolution were not available during the time the wiggler was being tested, so another normalization method had to be devised.

Another problem with normalizing the test data is that the acoustic pulse envelope could change slightly from pulse to pulse. The wire was pulsed at 0.1 Hz, so standing waves were damped out and not a factor. The likely source is a timing variation of the digitizing oscilloscope trigger caused by noise interfering with the acoustic signal. For example, an early trigger caused by interference between the noise and the acoustic pulse would result in the acoustic signal being displayed earlier than expected. The next pulse would probably trigger at a different point in the wave train and cause the average envelope to change with each pulse and take longer to reach steady state. The digitizing oscilloscope was only able to send 512 data points to the computer. Since the pulse displayed on the oscilloscope normally included a portion of the pulse reflected from the near pulley (Figure 11), only four to five data points were available to define each of the 65 wiggler periods in the primary acoustic pulse. A small change in the pulse phase could therefore have a great effect on the pulse envelope. As the pulse enveloped was averaged,

the phase interference would decrease the envelope amplitude and therefore decrease the centroid of the individual oscillations.

The normalization factor could be obtained by noting that the electron path for a perfectly injected electron beam in a linear undulator is [chap 5],

$$x = -\frac{K\lambda_o}{\sqrt{2}\pi\gamma}\sin(\omega_o t), \tag{20}$$

where $\omega_o = k_o c$. The corresponding velocity in the x-direction is,

$$\dot{x} = -\frac{K\lambda_o\omega_o}{\sqrt{2}\pi\gamma}\cos(\omega_o t). \tag{21}$$

This is related to the angular deflection of the electron beam by,

$$\theta_{\perp max} = \frac{\dot{x}_{max}}{c} = \sqrt{2}\frac{K}{\gamma}, \tag{22}$$

where $\dot{x}_{max} = \sqrt{2}Kc/\gamma$ is the maximum velocity in the x-direction. For the CEBAF IR parameters of $K \approx 0.99$ and $\gamma \approx 87.8$, $\theta_{\perp max} \approx 16$ mrad. Using the maximum peak-to-peak photodetector voltage to minimize the effect of the phase errors caused by the oscilloscope, and $\theta_{\perp max}$, the output of the photodetector can be scaled to provide normalized data values. Figure 12 shows the normalized first integral which indicates the electron beam angular deflection along the undulator.

The wiggler magnet correction coils were then energized and adjusted to remove the entrance and exit half-period magnetic kicks, with the normalized data shown as Figure 13. Note that the angular deflection increases steadily from $N \approx 20$ to $N \approx 30$, or about 60 to 100 cm along the wiggler, which indicates that the rate of change in the electron beam error will increase.

The second integral of the electron beam motion can be obtained by numerically integrating the first integral data. Figure 14 shows this integration, and the resulting electron beam path error of $\Delta x \approx 5.2$ mm, which is much greater than the electron beam

diameter of, $r_e \approx 0.4$ mm and the optical mode waist of, $w_o \sim 1$ mm. This again shows that some of the magnet pairs from $N \approx 20$ to $N \approx 30$ will require shimming or replacement to decrease the electron beam path error.

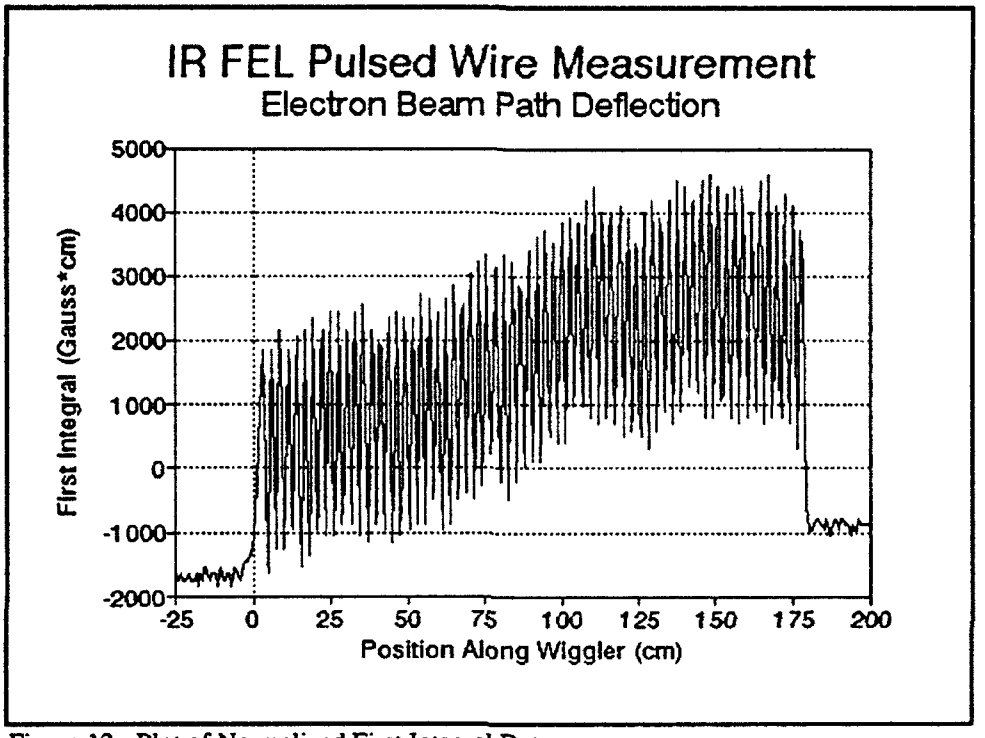

Figure 12 - Plot of Normalized First Integral Data.

The usual method of obtaining the second integral of the pulsed wire motion requires a longer electrical pulse, on the order of several milliseconds, to return an acoustic pulse of at least the wiggler length. For the 1.82 m CEBAF/NIST wiggler, a current pulse of at least 6 ms was needed. Since the acoustic wave propagates in both directions, reflections of the acoustic pulse from the pulley approximately 10 cm from the entrance end of the wiggler (Figure 7, right side) interfered with the primary acoustic signal. The pulley shown on the left side of Figure 7 did not pose a problem. This interference required that

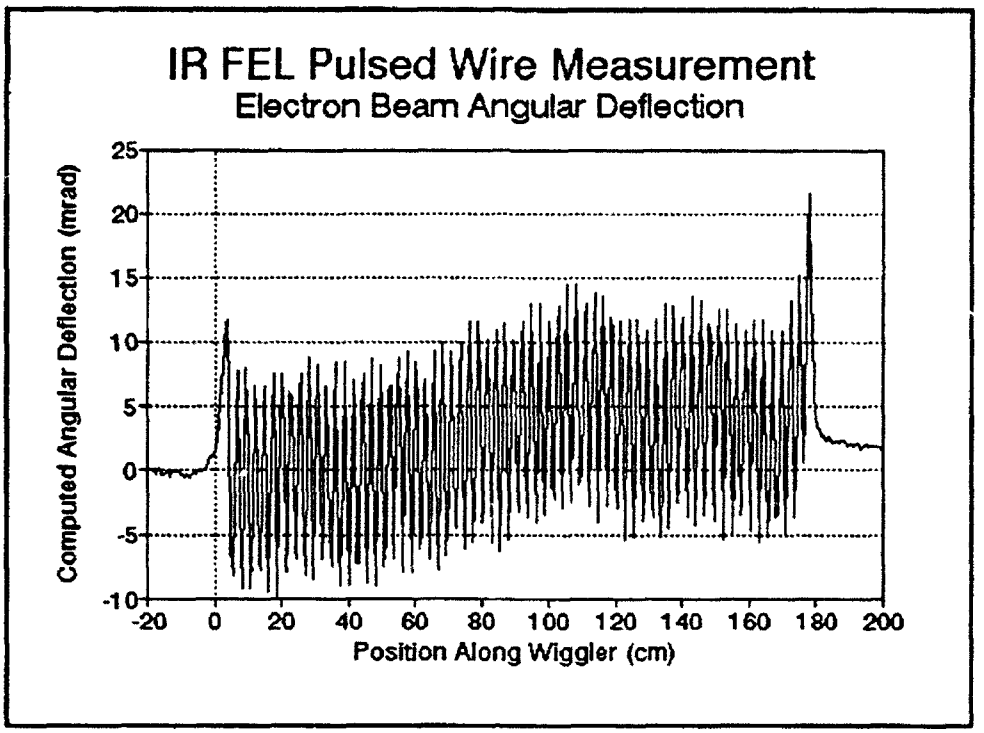

Figure 13 - First Integral Data With Entrance and Exit Magnetic Correction Coils Energized.

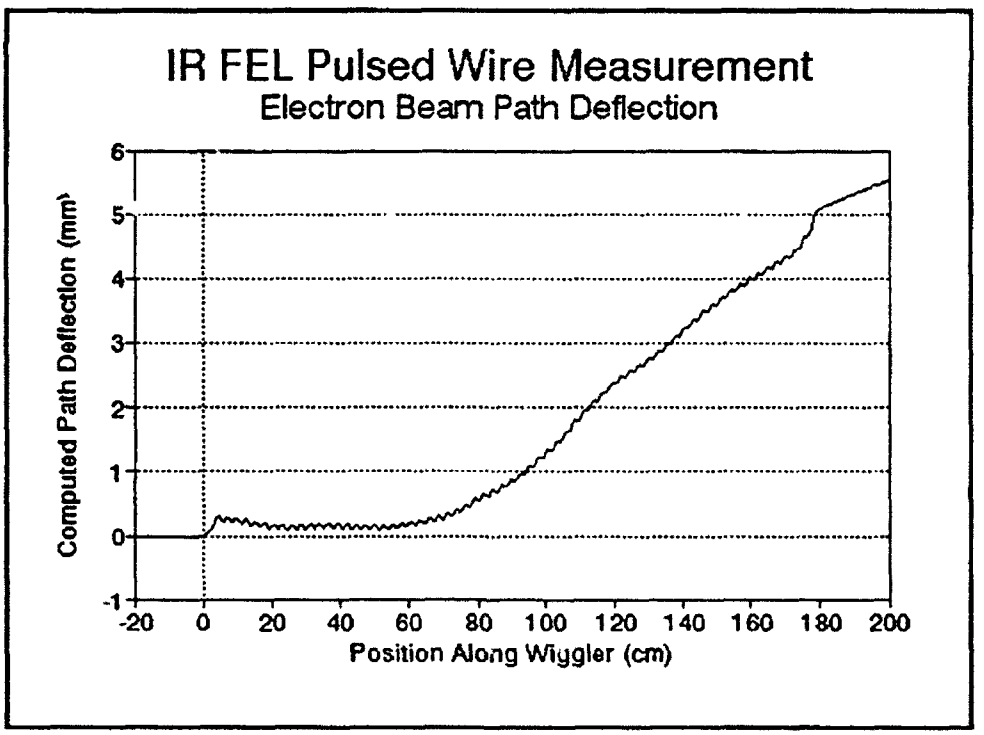

Figure 14 - Computed Second Integral Data With Entrance and Exit Correction Coils Energized.

numerical integration of the first integral data (Figure 13) be used to obtain the second integral (Figure 14). Mounting the pulley a longer distance from the wiggler end would have solved this problem, but was not possible because of space constraints in the wiggler testing area.

For the CEBAF UV FEL, the exit wiggler half would be tested in a similar manner to determine the net electron deflection through the entire undulator. This was not completed because of time constraints.

LIST OF REFERENCES

1. J. M. J. Madey, J. Appl. Phys. **42**, 1906 (1971); J. M. J. Madey, "Stimulated Emission of Radiation in Periodically Deflected Electron Beam", US Patent 3,822,410 (1974).

2. L. R. Elias, and others, Phys. Rev. Lett. **36**, 717 (1976).

3. D. A. G. Deacon, and others, Phys. Rev. Lett. **38**, 892 (1977).

4. C. Yamanaka, "Future Industrial Application of Free Electron Lasers", Nucl. Instr. and Meth., **A272** 257-263, North-Holland, Amsterdam (1988).

5. G. R. Neil, and others, "FEL design using the CEBAF linac," Nucl. Instr. and Meth., **A318** 212-215, North-Holland, Amsterdam (1992).

6. N. Bloembergen, and others, "Report to the American Physical Society of the study group on science and technology of directed energy weapons", *Reviews of Modern Physics*, v.59, No. 3 Part II, July 1987.

7. J. Bell, *Thunderball*, W. J. Schafer Associates, 1901 North Fort Myer Drive, Arlington, VA 22209, 1991.

8. R. Bradford, "High Energy Laser Weapon System (HELWEPS) for Anti-Ship Missile Defense," presented to the Naval Postgraduate School, Monterey, CA, 18 August 1992.

9. S. M. Wallace, and others, "Magnetic Field Error Measurement of the CEBAF (NIST) Wiggler Using the Pulsed Wire Method," presented at the 14th International Free Electron Laser Conference, Kobe, Japan, 23-28 August 1992.

10. S. M. Wallace, and others, "Magnetic Field Error Measurement of the CEBAF (NIST) Wiggler Using the Pulsed Wire Method," submitted to Nucl. Instr. and Meth., **AXXX**, xxxx-xxxx, 1992.

11. N. Friedman, *The Naval Institute Guide to World Naval Weapons Systems*, Naval Institute Press, Annapolis, MD, 81-82, 1989

12. "Loral to study laser anti-missile system," *Jane's Defense Weekly*, 19, 25 July 92

13. N. Friedman, "World Naval Developments," *Naval Institute Proceedings*, 118/9/1075, 123-124, Sept 1992.

14. J. S. Bermudez, Jr., "North Korea's Nuclear Progamme," *Jane's Intelligence Review*, 404, Sept 1991

15. A. L. Throop, and others, "Experimental Characteristics of a High-Gain Free Electron Laser Amplifier Operating at 8 mm and 2 mm Wavelengths," prepared for AIAA 19th Fluid Dynamics Plasma Division and Laser Conf., Honolulu, HI, 8-10 June 1987.

16. R. W. Warren, and others, "Recent Results fron the Los Alamos Free Electron Laser," Nucl. Instr. and Meth., **A259**, North-Holland, Amsterdam (1987).

17. K-J Kim and A. Sessler, "Free electorn Lasers: Present Status and Future Prospects," Science, Vol. 250, 5 October 1990.

18. Continuous Electron Beam Accelerator Facility, *High-Power UV and IR Free Electron Lasers Using the CEBAF Superconducting Accelerator*, Vol. 1, Newport News, VA, October, 1991.

19. W. B. Colson, "Classical Free Electron Theory", Chapter 5 in *Free Electron Laser Handbook*, W. B. Colson, C. Pellegrini and A. Renieri (eds.), North-Holland Physics, Elsevier Science Publishing Co. Inc., The Netherlands, 1990.

20. P. Elleaume, "Free Electron Laser Undulators, Electron Trajectories and Spontaneous Emission", Chapter 4 in *Free Electron Laser Handbook*, W. B. Colson, C. Pellegrini and A. Renieri (eds.), North-Holland Physics, Elsevier Science Publishing Co. Inc., The Netherlands, 1990.

21. W. B. Colson, IEEE J. Quantum Electron, **QE-17** (1981) 1417.

22. R. W. Warren, "Limitations on the Use of the Pulsed Wire Field Measuring Technique", Nucl. Instr. and Meth., **A272** 257-263, North-Holland, Amsterdam (1988).

23. R. G. Johnson, and others, "The NIST-NRL Free Electron Laser Facility", Free Electron Lasers and Applications, **1227** 14-25, SPIE, Bellington, WA, USA (1990).

24. R. W. Warren and C. J. Elliott, "A New System for Wiggler Fabrication and Testing", Paper delivered at Adriatico Research Conf. on Undulator Magnets for Synchrotron Radiation and Free Electron Lasers , 23-28 June 1987, submitted to Phys. Scr.

25. S. C. Gottschalk, and others, "Wiggler Error Reduction Through Shim Tuning", Nucl. Instr. and Meth., **A296** 579-587, North-Holland, Amsterdam (1990).

26. R. W. Warren and D. W. Preston, "Field Measurements in Pulsed Microwigglers", paper delivered at the 13th International Free Electron Laser Conference, 25-30 August 1991.

27. R. W. Warren, personal communication.

INITIAL DISTRIBUTION LIST

1.	Defense Technical Information Center Cameron Station Alexandria, VA 22304-6145	2
2.	Library, Code 52 Naval Postgraduate School Monterey, CA 93943-5002	2
3.	Professor William B. Colson, Code PH/Cw Department of Physics Naval Postgraduate School Monterey, CA 93943-5002	7
4.	Dr. George Neil CEBAF 12000 Jefferson Ave. Newport News, VA 23606	3
5.	Professor K. E. Woehler, Code PH/Wh Department of Physics Naval Postgraduate School Monterey, CA 93943-5002	1